Hindawi
International Journal of Energy Research
Volume 2023, Article ID 9889312, 13 pages
https://doi.org/10.1155/2023/9889312

Research Article

Highly Efficient Dehydrogenation of Ammonia Borane over Reduced Graphene Oxide-Supported Pd@NiP Nanoparticles at Room Temperature

Lan Yang,[1] Zien Liu,[1] Bin Qu,[1] Ye Tao ,[1] and Yihui Liu[2]

[1]*Hubei Research Center for New Energy & Intelligent Connected Vehicle, Wuhan University of Technology, Wuhan 430070, China*
[2]*Hubei Key Laboratory of Advanced Technology for Automotive Components & Hubei Collaborative Innovation Center for Automotive Components Technology, Wuhan University of Technology, Wuhan 430070, China*

Correspondence should be addressed to Ye Tao; tao-ye@whut.edu.cn

Received 22 September 2022; Revised 27 December 2022; Accepted 28 December 2022; Published 3 February 2023

Academic Editor: Arun Thirumurugan

Transition metal phosphating Pd@NiP nanoparticles supported by reduced graphene oxide were successfully synthesized by a one-step in situ synthesis method. The Pd@NiP/rGO nanoparticles were characterized by powder X-ray diffraction (XRD), X-ray photoelectron spectroscopy (XPS), transmission electron microscopy (TEM), confocal Raman spectroscopy (Raman), Fourier transform infrared spectroscopy (FT-IR), and BET. Compared with Pd/rGO and Pd@Ni/rGO, $Pd_1@Ni_{12.5}P_{40}$/rGO exhibited stronger catalytic activity, with TOF value reaching 133.33 min^{-1} and activation energy (Ea) of 29.31 kJ mol^{-1}. This excellent catalytic performance may be related to the good dispersion of nanoparticles and the synergistic electron interactions between transition metal phosphating compounds.

1. Introduction

Hydrogen energy is one kind of new energy promoted by various countries at present. Compared with traditional energy, hydrogen energy has the advantages of very high energy value, wide application range, and clean and pollution-free [1–3]. Hence, interest in developing suitable hydrogen storage materials has grown rapidly over the past few decades. However, the efficiency and safety of hydrogen storage still exist as the biggest challenges for the future development of the hydrogen economy. So far, some good hydrogen storage materials such as metal hydrides [4, 5], adsorption materials [6, 7], and chemical hydrides have been extensively studied [8–10]. Chemical hydrides containing boron and nitrogen have come into notice for the high hydrogen content and good hydrogen release kinetics. Ammonia borane (NH_3BH_3, AB) has a very high hydrogen content (19.6 wt%) and high aqueous stability, which is considered as a promising portable and attractive hydrogen storage material [11, 12]. As can be seen from equation (1), 3 mol of H_2 can be released for 1 mol of AB hydrolysis with an appropriate catalyst [13]. It is well known that noble metals like Ru, Pd, Pt, and Rh have the highest catalytic performance towards the hydrolysis of AB; however, their rarity and high price have seriously hindered their popularity and application [14–17]. Therefore, the development of efficient, economical, and stable AB hydrolysis catalysts is essential but still a great challenge.

$$NH_3BH_3 + 2H_2O \xrightarrow{Cat} NH_4^+ + BO_2^- + 3H_2 \quad (1)$$

As we all know that the catalytic activity of metal catalysts largely relies on the dispersity of active metals. In order to obtain high-performance catalysts, surfactants and high surface area carrier materials have been used to prepare various catalysts [18]. We added graphene oxide as a carrier in the

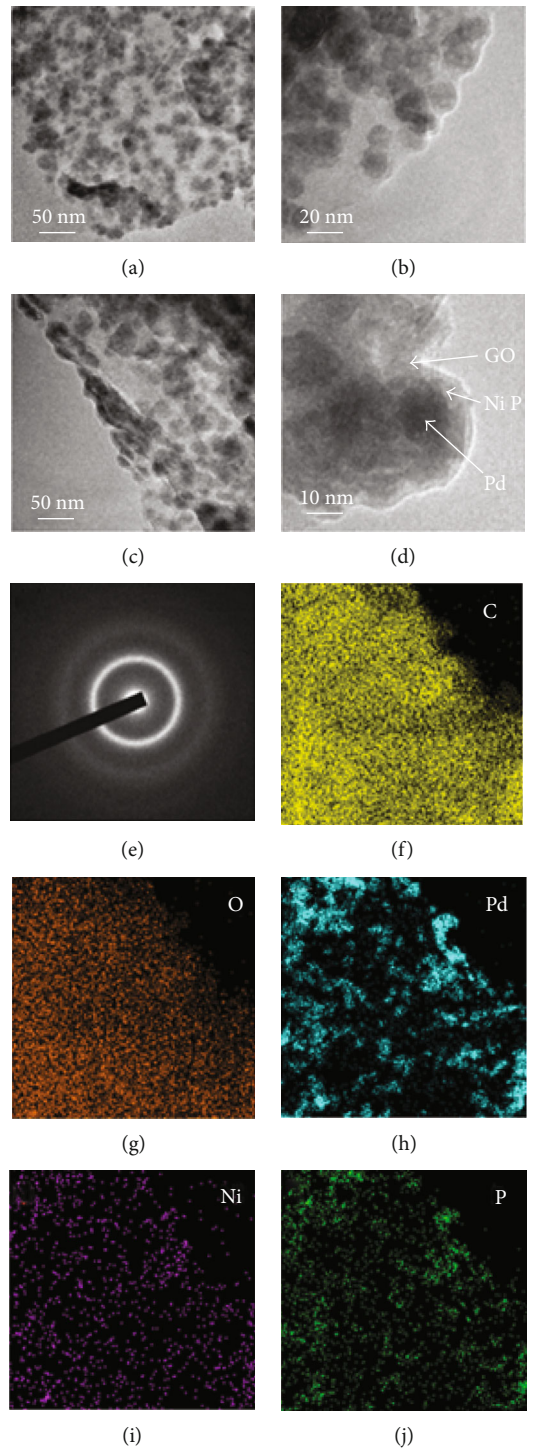

Figure 1: (a–d) TEM images of $Pd_1@Ni_{12.5}P_{40}$/rGO at different magnifications. (e) SEAD images of $Pd_1@Ni_{12.5}P_{40}$/rGO nanoparticles. (f–j) EDS mapping images of $Pd_1@Ni_{12.5}P_{40}$/rGO nanoparticles.

synthesis process, so that the catalyst particles may have better dispersion and more active sites. Graphene is a single-atom thick carbon material with excellent thermochemical stability, high specific surface area, and electrical conductivity, making it an ideal carrier for the fixation and growth of nanoparticles [19]. In addition, transition metal phosphides (TMPs) have unique charged properties (transition metal positively charged and phosphorus negatively charged) and have attracted particular attention in hydrogen evolution reactions (HER) and hydrodesulfurization (HDS), possibly due to its catalytic mechanism that is similar with hydrogenase resulting in high catalytic activity [20–24]. In recent years, many scholars have also studied transition metal phosphating as a kind of efficient catalyst for hydrogen storage materials. For example, Du et al. reported the synthesis of amorphous NiP/rGO hybrids of transition metal phosphide using one-pot coreduction, and

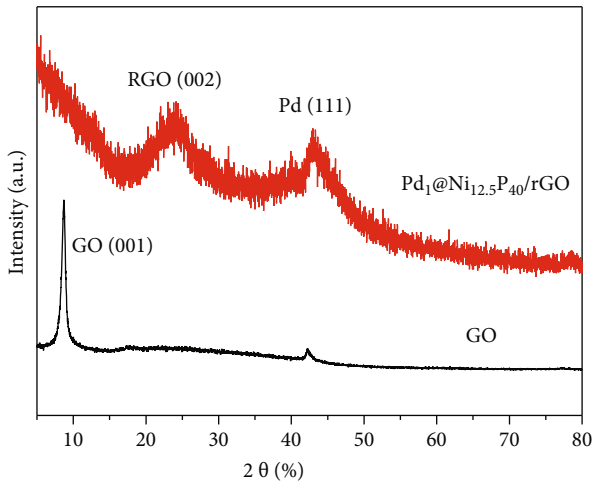

Figure 2: XRD images of $Pd_1@Ni_{12.5}P_{40}$/rGO and GO.

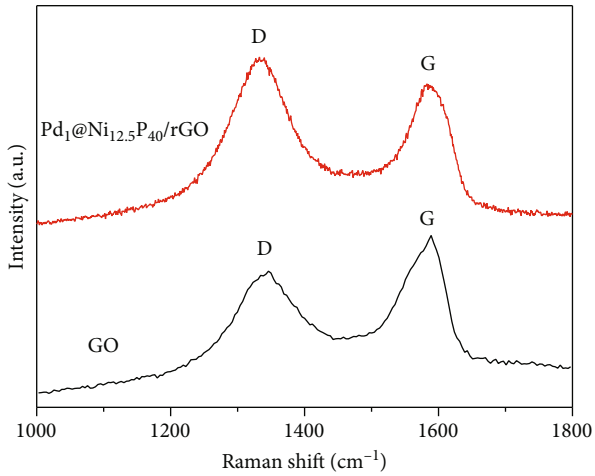

Figure 3: Raman spectra of $Pd_1@Ni_{12.5}P_{40}$/rGO and GO.

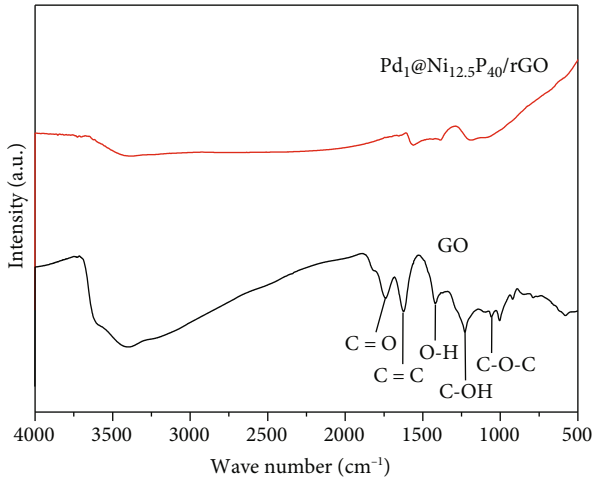

Figure 4: FT-IR spectra of $Pd_1@Ni_{12.5}P_{40}$/rGO and GO.

the catalytic property of NiP/rGO NPs towards the hydrolysis of AB is also studied. This excellent performance may be related to the synergistic electron interaction between nickel and phosphorus [25]. Peng accounted the synthesis of nanostructure Ni_2P using $Ni(OH)_2$ powder and NaH_2PO_2 in argon at 543 K. The mechanism study showed that the binding of catalyst surface with the substrate molecules is the key factor to improve catalytic activity [26].

In this study, using MeAB as reducing agent and $PdCl_2$, $NiCl_2$, and NaH_2PO_2 as precursors, the reduced graphene oxide-supported Pd@NiP core-shell nanoparticles were synthesized by one-step method and used as an efficient and stable ammonia borane catalyst for hydrogen production. Firstly, Pd@NiP/rGO core-shell nanoparticles were synthesized and characterized. Thanks to the effective and efficient doping of P and the synergistic electron effect between Ni and P, the synthesized Pd@NiP/rGO nanoparticles exhibit stronger catalytic activity than the phosphorus-free nanoparticles for the hydrolysis of AB. The catalyst has excellent catalytic activity, the TOF value is 133.33 min^{-1}, and the activation energy (Ea) value is 29.31 $kJ{\cdot}mol^{-1}$. This simple and fast synthesis way can also be applied to the synthesis of other graphene-supported transition metal phosphating catalysts.

2. Experimental

2.1. GO Preparation. GO was prepared by following the modified Hummers method [27, 28], adding 360 mL H_2SO_4 and 40 mL H_3PO_4 (9 : 1) into the round-bottom flask in an ice bath, and add 18 g $KMnO_4$ powder in batches with slow stirring, then heat to 50°C, and maintain the stirring reaction for 12 h. After the reaction, cool to room temperature (RT), pour the solution above into 400 mL deionized water comprising 3 mL 30% H_2O_2 in an ice-bath, and then add H_2O_2 under stirring until the solution becomes a constant yellow. The products were obtained by centrifuging and washing with 30% diluted HCl, deionized water, and ethanol for three times, respectively. GO powder was obtained by vacuum drying at RT for 12 h.

2.2. Preparation of MeAB. The synthesis method of MeAB is the same as in the reference [29], at room temperature, and 3.783 g $NaBH_4$ and 6.752 g CH_3NH_3Cl were placed into a 500 mL two-port round-bottom flask. Nitrogen was inserted into one mouth of the round-bottom flask, and 200 mL tetrahydrofuran was added under agitation. After 12 hours of reaction at RT, the initial product was obtained by extracting and evaporating the solvent. Then, the initial product is added to the ether under an ice bath and stirred for 2 hours. Finally, highly purified MeAB was also obtained by filtration and evaporation.

2.3. In Situ Synthesis of Pd@NiP/rGO Catalysts. For $Pd_1@Ni_{12.5}P_{40}$/rGO NPs, 10 mg of GO powder was placed in a two-necked flask, and 5 mL of deionized water was added to disperse the mixture by ultrasound. 0.5 mL $PdCl_2$ solution (0.01 mol/L), 0.625 mL $NiCl_2$ solution (0.1 mol/L), and 2 mL NaH_2PO_2 solution (0.1 mol/L) were added to the flask. MeAB solution was added by a constant pressure drip funnel on one neck, and the other neck is connected to a

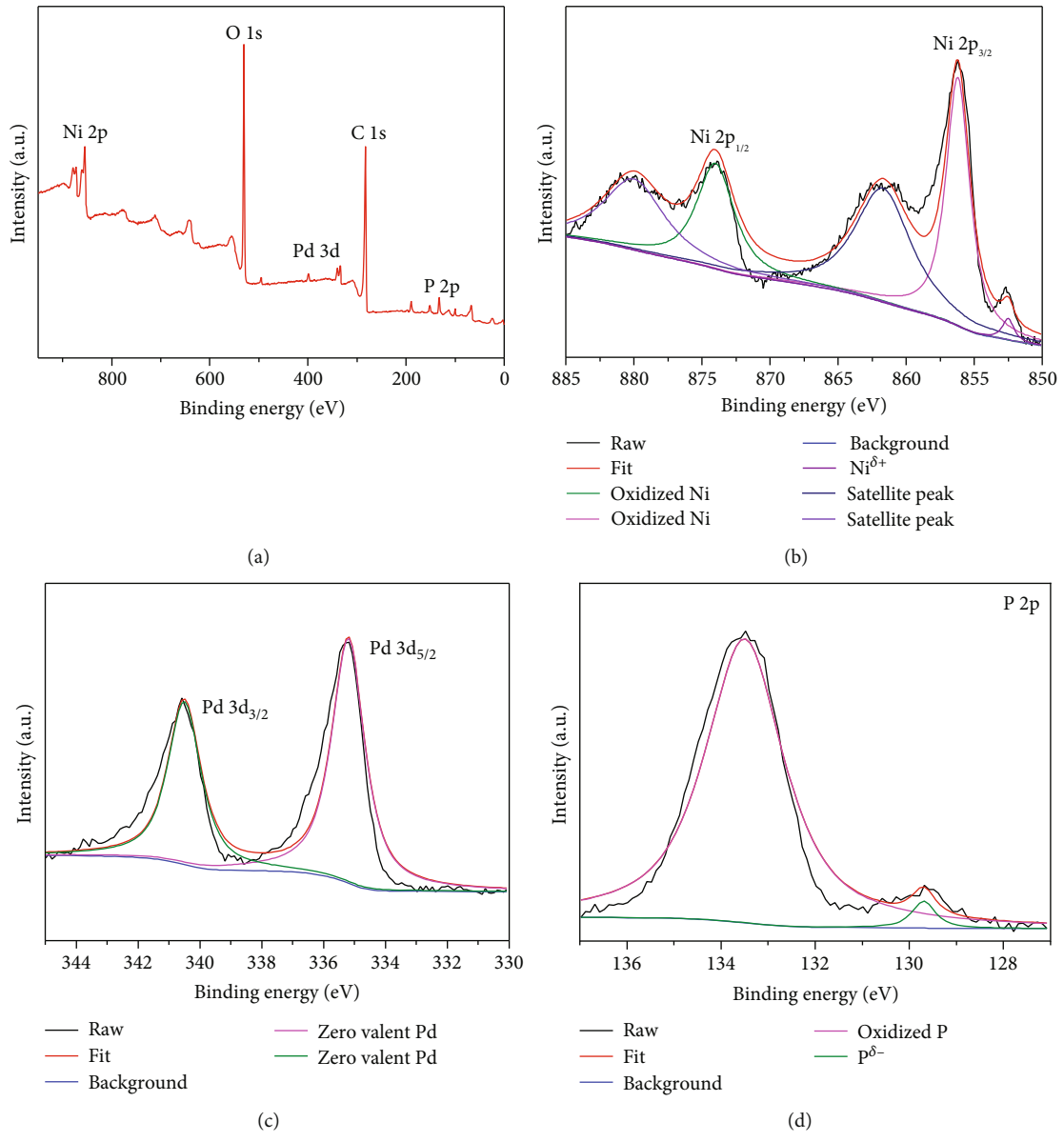

Figure 5: Continued.

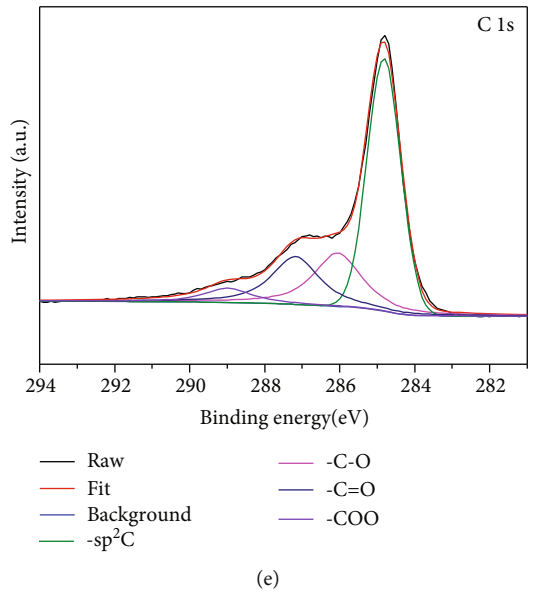

Figure 5: (a) The XPS survey spectrum of $Pd_1@Ni_{12.5}P_{40}$/rGO. (b–d) XPS spectra of Pd 3d, Ni 2p, P 2p, and C 1 s.

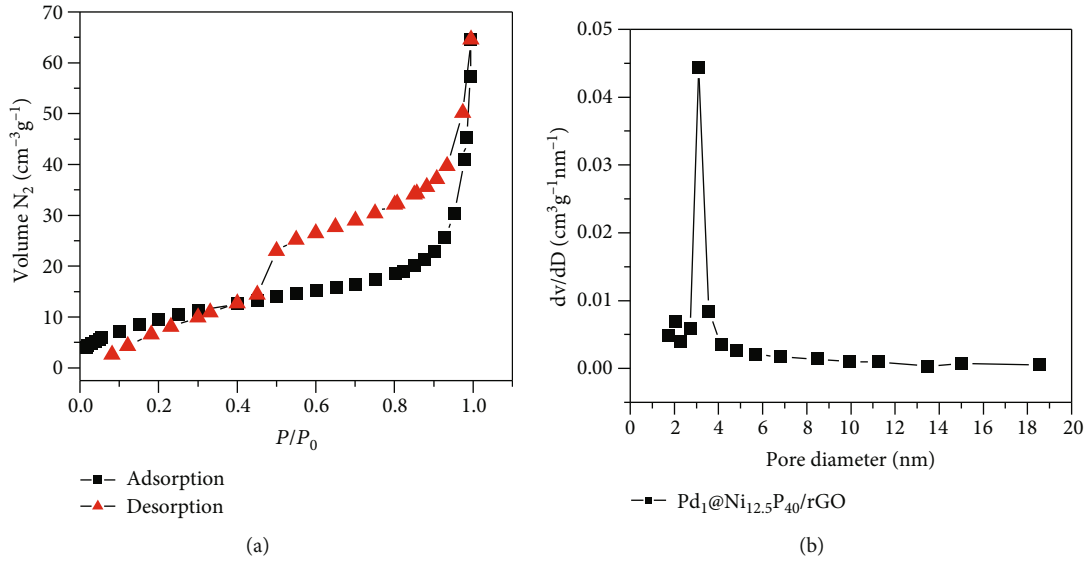

Figure 6: (a) N_2 adsorption and desorption images of $Pd_1@Ni_{12.5}P_{40}$/rGO. (b) Aperture distribution images of $Pd_1@Ni_{12.5}P_{40}$/rGO.

tube of gas quantity tube, which is used to detect gas generation and measure the volume of produced gas. Use a syringe to add 1 mL MeAB solution (1 mol/L) to a constant pressure drop funnel and cover with a glass stopper. The reaction begins when MeAB solution drops into the solution in the flask. The generated hydrogen is put into the gas burette by the catheter. When no bubbles are generated in the gas tube, the reaction is complete, and the precursor has been reduced completely. The catalyst was obtained by filtrating, washing, and drying.

In order to optimize the catalyst for higher catalytic activity to the hydrolysis of AB, Pd@NiP NPs with different composition are synthesized by a similar method, while keeping the molar ratio of Pd to AB (n(Pd)/n(AB)) at 0.005. The mole ratios of Ni/Pd are 0, 2.5, 5, 7.5, 10, 12.5, and 15, and the mole ratios of P/Pd are 0, 10, 20, 30, 40, and 50.

2.4. Materials Characterization. X-ray diffraction (XRD) was used to characterize the crystal structure of the material. The XRD pattern was obtained by Empyrean X-ray diffractometer with a Cu Kα as the radiation source ($\lambda = 0.154178$ nm), the scan velocity was 8°/min, and the angle of 2θ ranged from 5 to 80 degrees. The microstructure was obtained by JEM-2100F and JEM-ARM200F field-emission HETEM with EDAX Elite T energy spectrometer at 200 kV. Before testing, a small amount of powder samples was dispersed into ethanol by ultrasonic wave to prepare TEM samples,

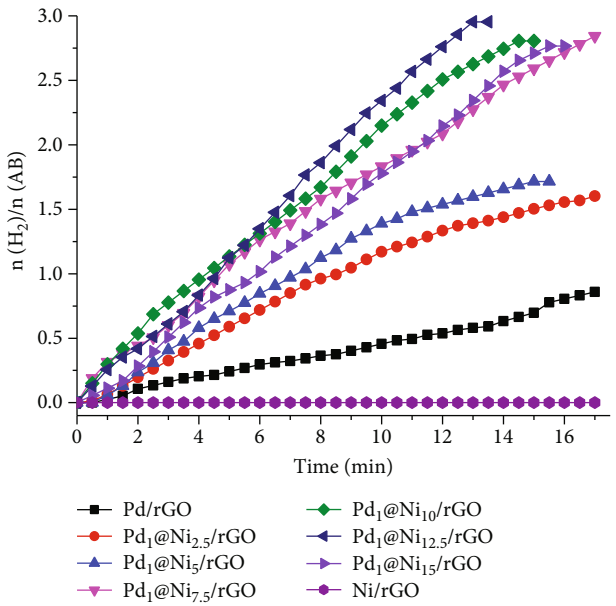

Figure 7: Hydrolysis of AB catalyzed by Pd@Ni/rGO with different Pd:Ni.

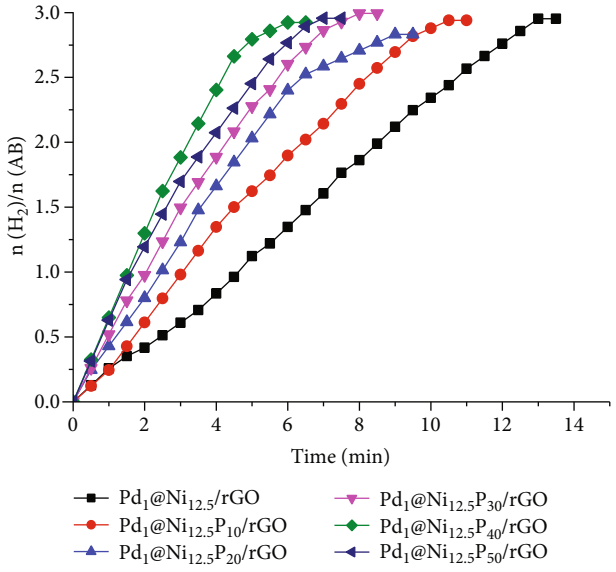

Figure 8: Hydrolysis of AB catalyzed by Pd@NiP/rGO with different quantity of phosphorus, $(n(\mathrm{Pd})/n(\mathrm{AB}) = 0.005)$.

and then, a drop of suspended liquid was dropped onto a 300-mesh copper net for measurement. FT-IR spectra were obtained at RT using a Nicolet 670 spectrometer (Thermo Fisher Scientific, USA) in the wave number range of 4000 to 400 cm^{-1}. Raman spectra in the range of 800 to 2000 cm^{-1} were obtained using a Renishaw confocal micro-Raman spectrometer excited by a laser beam at 514.5 nm. XPS spectra were surveyed by ESCALAB 250Xi X-ray photoelectron spectrometer. The element content was verified by ICP-OES (Prodigy 7). BET was scanned with the ASAP 2020 to test specific surface area and pore volume.

2.5. Catalytic Activity Test. The synthesized Pd@NiP/rGO nanoparticle catalyst was placed in a two-necked flask, one port of the flask was used to add ammonia borane aqueous solution (1 mmol ammonia borane dissolved in 1 mL water), another port is connected to a eudiometer to monitor gas production, and the reaction stops when no H_2 is produced. Keep the amount of AB at 1 mmol and calculate the catalytic rate of this catalyst by testing the catalysts with different concentrations $(n(\mathrm{Pd})/n(\mathrm{AB}) = 0.005, 0.006, 0.007, 0.008)$ at RT and determine whether the reaction is a first-order reaction. According to the requirements of the Arrhenius equation, the ratio of the molar amount of the catalyst to the molar amount of ammonia borane $(n(\mathrm{Pd})/n(\mathrm{AB}) = 0.005)$ was kept constant; the catalytic reaction was determined by the water bath of the magnetic stirrer temperatures during the process (298 K, 303 K, 308 K, and 313 K), and we can calculate the Ea value of the reaction. In order to measure the cyclic durability of the catalyst for catalyzing the hydrolysis of AB, the same amount of AB was added to continue the reaction after the last catalytic reaction under the same conditions, and the reaction was repeated 5 times. To calculate the conversion frequency (TOF) value of the hydrolysis of AB, the following formula is used:

$$\mathrm{TOF} = \frac{\mathrm{PV/RT}}{n_{\mathrm{Pd}} * t}, \tag{2}$$

where V is the volume of hydrogen, P is the atmospheric pressure, T is the temperature of the reaction, R is the molar gas constant, n_{Pd} is the molar mass of Pd, and t is the reaction time.

3. Results and Discussion

3.1. Synthesis and Characterization. During the synthesis of reduced graphene oxide-supported Pd@NiP core-shell nanoparticles, the MeAB solution was added to the aqueous solution which contained $PdCl_2$, $NiCl_2$, NaH_2PO_2, and GO. During the synthesis, due to the low reduction potentials of Ni^{2+} and $H_2PO_2^-$ ($E_0(\mathrm{Ni^{2+}/Ni}) = -0.25$ eV vs. SHE and $E_0(\mathrm{H_2PO_2^-/P}) = -0.508$ eV vs. SHE), MeAB with weak reducibility cannot reduce them, but it can reduce the Pd^{2+} which has high reduction potential ($E_0(\mathrm{Pd^{2+}/Pd}) = +0.915$ eV vs. SHE) to form Pd core. The Pd-H bond reduces Ni^{2+} and $H_2PO_2^-$ [30], which makes it continuously grow on the surface of the Pd core to deposit a NiP shell, and finally, Pd@NiP core-shell nanoparticles are obtained.

To verify the morphological characteristics of the catalyst, the microstructure of $Pd_1@Ni_{12.5}P_{40}$/rGO nanoparticles was characterized by TEM. In Figures 1(a)–1(c), the catalyst nanoparticles synthesized in situ by one-step method are uniformly dispersed on the graphene oxide carrier, and the light-colored folds on the bottom layer are graphene oxide carriers, which can be clearly seen; seeing its edge profile shows that graphene oxide can effectively prevent the aggregation of particles. In Figure 1(d), at a larger magnification, the obvious contrast between the core and the shell can be clearly observed; the black core is Pd, and the light gray shell is NiP, indicating that Pd is first reduced by MeAB, and

Table 1: Comparison of activities and Ea of different catalysts for hydrogen generation from AB hydrolysis.

Catalyst	TOF (mol H_2 Mol^{-1} catalyst min^{-1}) M = Ru, Pd	Ea (kJ Mol^{-1})	References
Pd(0)/SiO_2–$CoFe_2O_4$	254	52	[45]
$Ni_{0.74}Ru_{0.26}$ alloy	194.8	37.18	[46]
Pd@NiP	133.33	29.31	This study
CoNi/MCNTs	128	52.1	[47]
Pd@Co@P/rGO	127.57	39.05	[48]
$Pd_{0.6}Co_{0.2}Ag_{0.2}$/AC	110.4	26.84	[49]
$Ni^0/CoFe_2O_4$	38.3	62.7	[50]
Pd@Co/graphene	37.4	/	[51]
rGO-$Ni_{30}Pd_{70}$	28.7	45	[52]
Pd/S-1-in-K	14.27	39.2	[53]
NiP/rGO	13.3	34.7	[25]
p(AMPS)-Ni	0.54	52.8	[54]

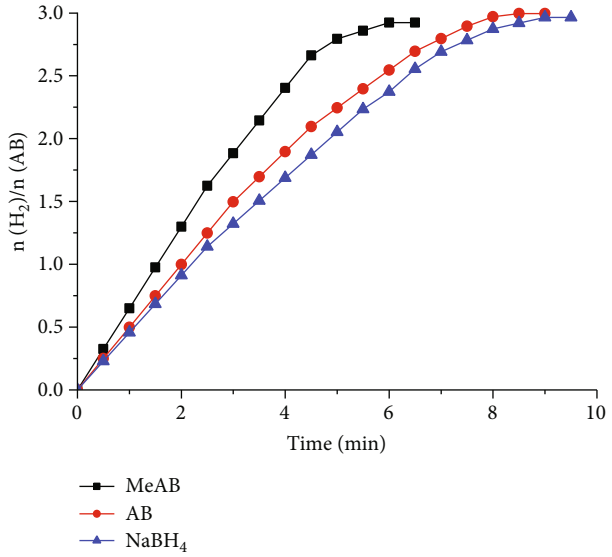

Figure 9: Hydrolysis of AB catalyzed by Pd@NiP/rGO obtained with different reducing agents.

then, as the seed of the core, it helps to promote the reduction of Ni^{2+} and $H_2PO_2^-$ to form a shell. The SAED result (Figure 1(e)) shows that $Pd_1@Ni_{12.5}P_{40}$/rGO NPs are polycrystalline, and the lattice spacing was calculated to be 0.224 nm, which is consistent with the Pd (111) crystal face. In order to determine the elemental composition and distribution of the nanoparticles, the EDS mapping images of $Pd_1@Ni_{12.5}P_{40}$/rGO are determined in Figures 1(f)–1(j). The presence and uniform distribution of Pd, Ni, and P were confirmed by the EDS mapping images. In addition, the distribution area of Ni and P is bigger than that of Pd, which can further indicate the existence of a core-shell structure.

Figure 2 shows the XRD images of $Pd_1@Ni_{12.5}P_{40}$/rGO and GO. It can be seen from the figure that there is a distinct diffraction peak at 43°. According to the comparison of the PDF# 88-2335 card, this peak is Pd (111) plane, which is consistent with the SAED result. No diffraction peaks of Ni appear in the images of $Pd_1@Ni_{12.5}P_{40}$/rGO, which may be due to the amorphous nature of Ni in the composites. In addition, compared with the spectrum of GO, the peak of GO (001) at 8.4° disappeared, and the peak of rGO appeared at 23.5° in the spectrum of $Pd_1@Ni_{12.5}P_{40}$/rGO, which indicated that GO has been completely reduced and rGO is formed. As can be seen from Figure 3, two distinct characteristic peaks can be observed in the Raman spectra of GO and $Pd_1@Ni_{12.5}P_{40}$/rGO at both 1342 cm^{-1} and 1589 cm^{-1}, which denote the D peak and G peak of the carbon material, respectively. The D-band is caused by GO disorder caused by defects such as vacancies, grain boundaries, and amorphous carbon, and the G-band is caused by E_{2g} phonons of C sp^2 in a two-dimensional hexagonal lattice [31, 32]. The intensity ratio of D peak and G peak (I_D/I_G) is used to

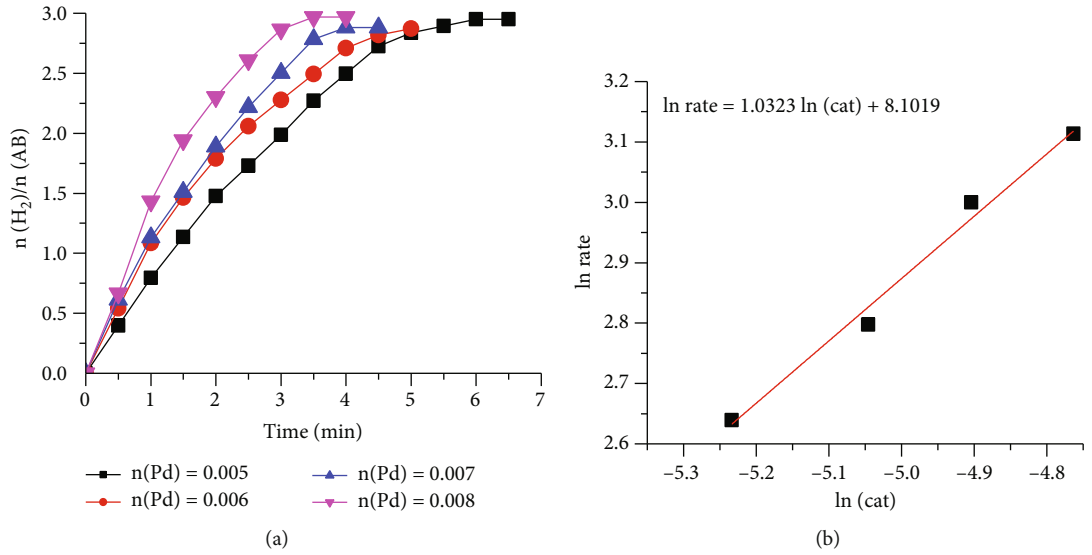

FIGURE 10: (a) Time plots of catalytic dehydrogenation of AB (1 mmol) by $Pd_1@Ni_{12.5}P_{40}$/rGO catalyzed at different catalyst concentration. (b) Logarithmic plot of hydrogen generation rate versus the concentration of $Pd_1@Ni_{12.5}P_{40}$/rGO.

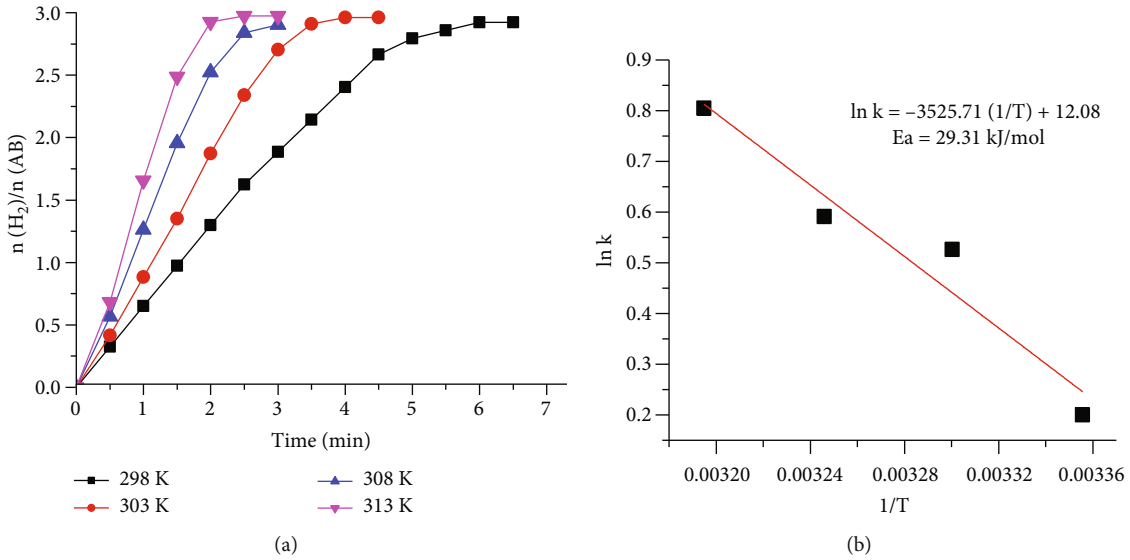

FIGURE 11: (a) Time plots of catalytic dehydrogenation of AB (1 mmol) catalyzed by $Pd_1@Ni_{12.5}P_{40}$/rGO at 298-313 K. (b) Arrhenius plot obtained from the data in Figure 11(a).

describe the degree of defect and graphitization of carbon materials [33]. The I_D/I_G of $Pd_1@Ni_{12.5}P_{40}$/rGO and GO are 1.01 and 1.29, which means that GO was successfully reduced to rGO during the reaction. The Fourier transform infrared spectra of $Pd_1@Ni_{12.5}P_{40}$/rGO and GO are shown in Figure 4. The strong wide band of GO at 3405 cm^{-1} is attributed to the moisture absorption of graphene oxide. The C=O stretching band of carbonyl or carboxyl group at 1736 cm^{-1} is weak. The peak value at 1619 cm^{-1} is related to the skeleton vibration of unoxidized graphite domains and the vibration of adsorbed water. The peaks at 1228 cm^{-1} and 1058 cm^{-1} are related to the C-OH vibration and the deformation of the C-O band in carboxylic acids, respectively [34]. In the FTIR result of $Pd_1@Ni_{12.5}P_{40}$/rGO, the peaks of C=O, C-OH, and C-O are disappeared, which further verified the reducing of GO during the reaction [35].

The composition and chemical valence of transition metal phosphide nanoparticles supported by GO were detected by XPS analysis. Figure 5(a) shows the full spectrum of $Pd_1@Ni_{12.5}P_{40}$/rGO nanoparticles. The signals of Pd, Ni, P, C, O, and other elements are clearly visible, indicating that Pd, Ni, and P elements have been successfully introduced into the composite. In Figure 5(b), the two obvious peaks at 335.1 eV and 340.4 eV represented Pd $3d_{5/2}$ and Pd $3d_{3/2}$ with zero valence state Pd, respectively. Figure 5(c) represents the peaks of Ni 2p, and the two peaks at 856.2 eV and 874.1 eV represent the oxidized Ni $2p_{3/2}$ and Ni $2P_{1/2}$, respectively [36]. These results indicate that Pd as the core

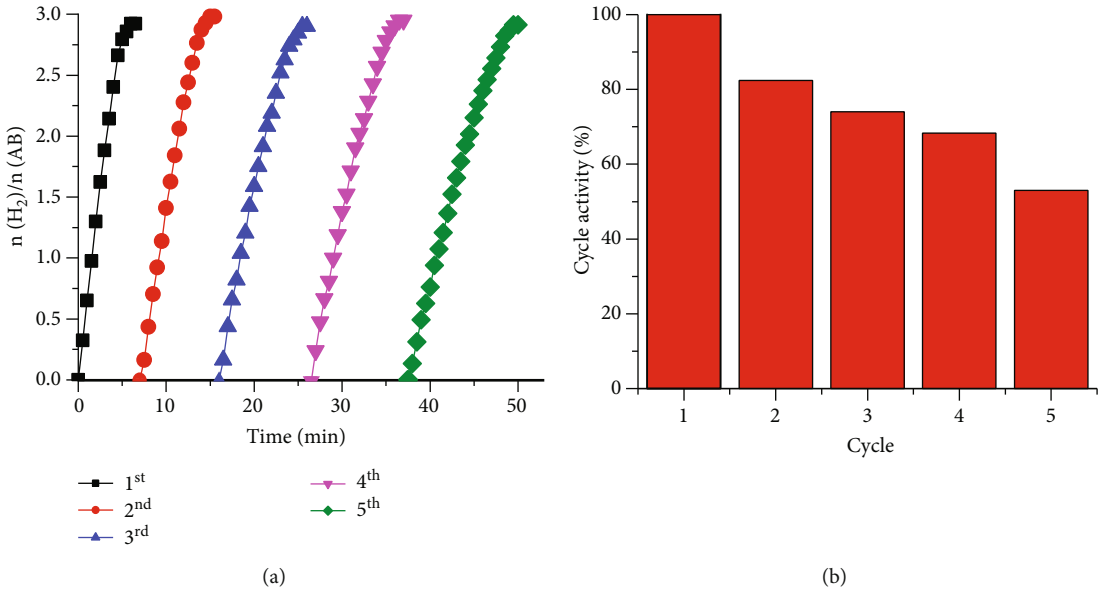

FIGURE 12: (a) Time plots of catalytic dehydrogenation of AB (1 mmol) continuously catalyzed by $Pd_1@Ni_{12.5}P_{40}$/rGO for five cycles. (b) Histogram of catalytic activity as a percentage of initial activity after each cycle.

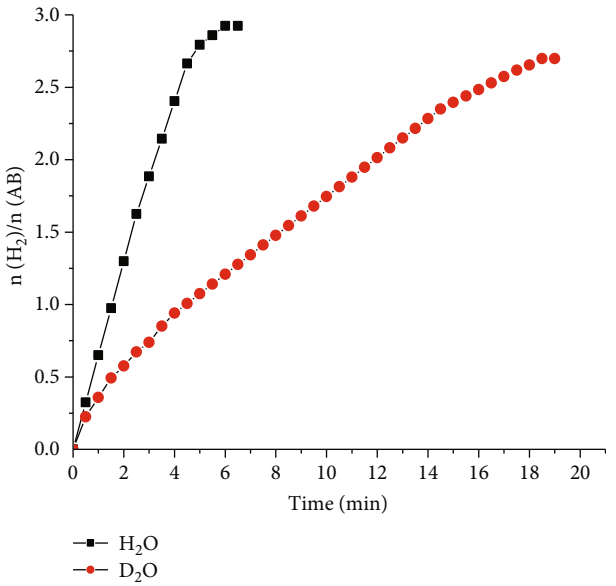

FIGURE 13: Hydrolysis of AB catalyzed by Pd@NiP/rGO with H_2O and D_2O.

is stable, so it is not oxidized, whereas the surface nickel is easily oxidized [37]. In Figure 5(c), there is a peak at 852.4 eV belonging to $Ni^{\delta+}$, which shows a positive displacement of 0.2 eV compared with the peak of metal Ni at 852.2 eV, with a small positive charge ($Ni^{\delta+}$, $0 < \delta < 2$) [38]. Figure 5(d) shows the XPS spectrum of P 2p. The peak at 129.7 eV is very close to the zero-valence P, indicating that P atoms in nanoparticles have marginal negative charge ($P^{\delta-}$, $0 < \delta < 1$) [39]. The other peak at 133.5 eV belongs to the oxidation state P formed on the surface of the catalyst due to air exposure [40]. These results indicate that there is a strong electron transfer between Ni and P, which is the key to improve the catalytic activity of the catalyst [41]. According to existing literature reports, hydrogenase has high HER activity, and the active sites are the pendant bases near the metal center [42]. The Ni(δ+) and the pendant base P(δ-) of $Pd_1@Ni_{12.5}P_{40}$/rGO nanoparticles have similar electronic structures to hydrogenase, so the high catalytic activity of $Pd_1@Ni_{12.5}P_{40}$/rGO may be related to the hydrogenase-like catalytic mechanism [43]. In Figure 5(e), XPS result for C1s of rGO indicates that four peaks at 284.8, 286.1, 287.2, and 289 eV are observed and identified as sp^2C, –C–O, –C=O, and –COO groups, respectively [44]. Figure 6 shows the nitrogen adsorption curve of $Pd_1@Ni_{12.5}P_{40}$/rGO sample calculated using the BET model, indicating that the $Pd_1@Ni_{12.5}P_{40}$ NPs occupy the orifice of the rGO. The surface area of $Pd_1@Ni_{12.5}P_{40}$/rGO was calculated to be 73.74 m^2g^{-1} using the Brunauer-Emmett-Teller (BET) model.

3.2. Catalytic Performance for the Hydrolysis of AB by Pd@NiP/rGO NPs. Pd@Ni/rGO catalysts with different ratios of palladium and nickel were synthesized using MeAB as a reducing agent, n(Pd)/n(AB) is fixed at 0.005, and the catalytic performance of the catalysts for AB hydrolysis was investigated. As shown in Figure 7, in the absence of Pd, MeAB cannot reduce Ni^{2+}, resulting in the inability to catalyze the hydrolysis and dehydrogenation of AB. When pure palladium particles are supported on graphene oxide, it takes about 42 minutes to fully release 3 equivalents of hydrogen by catalyzing the hydrolysis of AB. By changing the amount of Ni, Pd@Ni/rGO exhibited different catalytic activities. As the ratio of Ni:Pd increased from 2.5 to 12.5, the catalytic activity of the catalyst increased rapidly, and the catalytic activity decreased when the ratio continued to rise, which indicated that the best ratio of Pd to Ni in the Pd@Ni/rGO catalyst was 1 : 12.5.

To obtain catalysts with different phosphorus content, we control the phosphorus content by adding different doses of NaH_2PO_2 solution. Figure 8 shows the effect of different phosphorus contents on catalytic hydrolysis performance of the Pd@NiP/rGO catalysts. From the figure, it can be observed that the catalyst activity is greatly improved after adding phosphorus. In addition, the catalytic activity of the catalysts enhances with increasing the content of phosphorus and increasing the ratio of P:Pd from 0 to 40. The best ratio of Pd:P is 1 : 40, namely, $Pd_1@Ni_{12.5}P_{40}$/rGO. By calculation, the TOF value of the catalyst $Pd_1@Ni_{12.5}P_{40}$/rGO is 133.33 min^{-1}, which is higher than that of many Pd-based nanoparticles without P (as shown in Table 1). The mass loading of Pd@NiP nanoparticles and on reduced graphene oxide is 19.12 wt% which is calculated from the results of ICP-OES.

Figure 9 shows the curves of AB hydrolysis catalyzed by Pd@NiP/rGO nanoparticles gained by using different reducing agents (MeAB, AB, and $NaBH_4$). The activity of Pd@NiP/rGO NPs reduced by MeAB is significantly higher than the catalysts obtained by the reduction of AB and $NaBH_4$, and their catalytic activity is inversely proportional to the reducibility, further indicating that the reducibility of the reducing agent plays an important role in the synthesis of the catalyst, thus affecting the catalytic activity.

Figure 10 shows the hydrolysis and dehydrogenation curves of AB (1 mmol) catalyzed by $Pd_1@Ni_{12.5}P_{40}$/rGO nanoparticle catalysts with different concentrations at room temperature. The ratios of $n(\mathrm{Pd})/n(\mathrm{AB})$ are 0.005, 0.006, 0.007, and 0.008, respectively. The dehydrogenation rate is calculated by taking the linear part of the first segment with the most stable slope of each dehydrogenation curve. Each dehydrogenation rate corresponds to a point in the logarithmic graph, and the four points in the logarithmic graph are fitted to a straight line, which can be calculated when a slope of 1.0323 was obtained, which indicated that the $Pd_1@Ni_{12.5}P_{40}$/rGO nanoparticles catalyzed a first-order reaction of the AB hydrolysis process relative to the catalyst concentration. In order to get the activation energy (Ea) of the hydrolysis reaction catalyzed by $Pd_1@Ni_{12.5}P_{40}$/rGO nanoparticles, the reaction was carried out in at different temperature ranged from 298 K to 313 K. The value of the rate constant k is calculated from the dehydrogenation curve in Figure 11(a). Figure 11(b) plots the Arrhenius curve of the ln k of the catalyst as a function of $1/T$. It can be seen from the image that Ea for catalyzing the hydrolysis of AB is 29.31 kJ·mol^{-1}, which is lower than many reported catalysts shown in Table 1, indicating that the synthesized $Pd_1@Ni_{12.5}P_{40}$/rGO nanoparticle catalyst has preeminent catalytic performance towards the hydrolysis of AB.

The cycle durability of the catalyst is essential for practical application. In the catalytic hydrolysis process of AB, the cyclic stability of $Pd_1@Ni_{12.5}P_{40}$/rGO is shown in Figure 12. After five cycles of continuous catalytic hydrolysis of ammonia borane, $Pd_1@Ni_{12.5}P_{40}$/rGO nanoparticles still maintain 52.98% of the incipient catalytic activity. The catalytic activity and conversion rate remained good after the cycle, indicating that $Pd_1@Ni_{12.5}P_{40}$/rGO nanoparticles can be recycled for at least five times.

In order to further research the mechanism of hydrolysis AB catalyzed by $Pd_1@Ni_{12.5}P_{40}$/rGO, the isotope experiment was conducted by using D_2O as the solvent instead of H_2O. From Figure 13, the hydrolysis rate of AB in D_2O is much lower than that of H_2O as the solvent. The high kinetic isotope effect (KIE) of D_2O (kH/kD = 3.1) stated that the division of the O-H bond of water is the rate-determining step of the hydrolysis reaction, which was also consistent with previous research [55]. The interaction between H with positive charge in water and $P^{\delta-}$ can speed up the rate-determining step to obtain faster reaction kinetics. In this context, we can infer the possible mechanism of $Pd_1@Ni_{12.5}P_{40}$/rGO catalytic hydrolysis of AB when considering the report published earlier. At the start of AB hydrolysis, H_2O may offend AB to form $[H_3NBH_2H]$ H-OH species [12] and interact with Pd@NiP NPs sequentially. The B-H bond breaks subsequently, and the H atom shifts to the surface of Pd@NiP which leads to an increase in the oxidation capacity of the B-H bond; the synergistic effect makes this process easier. The H of B-H in ammonia borane with negative charge will have electric charge effect with $Ni^{\delta+}$[56]. The synergistic catalytic effects of the Ni and P may be the key to enhance the catalytic activity. At the same time, the water molecule splits into H^+ and OH^-, and one of H atom in AB is replaced by OH in water. Therefore, the two active H atoms provided by AB and H_2O combine to release H_2 molecules, and with that comes the creation of $BH(OH)_2NH_3$ and $B(OH)_3$ as the by-products.

4. Conclusion

Reduced graphene oxide-loaded Pd@NiP core-shell nanoparticles were synthesized by a one-step method as the catalyst for hydrogen production from hydrolysis of ammonia borane. The Pd@NiP/rGO core-shell nanoparticles were characterized by TEM, XRD, FTIR, Raman, XPS, and BET. The catalytic performance test shows that the synthesized Pd@NiP/rGO nanoparticles exhibit stronger catalytic activity than the phosphorus-free nanoparticles, which may be caused by the effective doping of phosphorus and the synergistic electron effect between Ni and P. The as-synthesized catalyst puts up splendid catalytic activity, with a TOF value of 133.33 min^{-1} and activation energy (Ea) of 29.31 kJ mol^{-1}. MeAB with weak reducibility has better control capability in reducing metal ions than AB and $NaBH_4$, so it can obtain catalyst with better catalytic activity. In addition, the results of the isotope experiment manifested that the division of the O-H bond of water was the rate-determining step of the hydrolysis reaction, and a detailed mechanism for the hydrolysis of AB catalyzed by nanoparticles was also put forward. Furthermore, the simple one-step synthesis method can be expanded to other graphene-supported transition metal phosphating core-shell nanoparticles.

Data Availability

The manuscript does not contain the original data.

Conflicts of Interest

The authors declare that they have no conflicts of interest.

Acknowledgments

This research was supported by the National Natural Science Foundation of China (Grant No. 21805217) and the Fundamental Research Funds for the Central Universities (WUT: 2019IVB014, 2021IVA014).

References

[1] S. Dunn, "Hydrogen futures: toward a sustainable energy system," *International Journal of Hydrogen Energy*, vol. 27, no. 3, pp. 235–264, 2002.

[2] Y. Karataş, T. Çetin, İ. N. Akkuş, Y. Akinay, and M. Gülcan, "Rh (0) nanoparticles impregnated ontwo-dimensionaltransition metal carbides,MXene, as an effective nanocatalyst for ammonia-borane hydrolysis," *International Journal of Energy Research*, vol. 46, no. 8, pp. 11411–11423, 2022.

[3] J. Nowotny, T. Bak, D. Chu, S. Fiechter, G. E. Murch, and T. N. Veziroglu, "Sustainable practices: solar hydrogen fuel and education program on sustainable energy systems," *International Journal of Hydrogen Energy*, vol. 39, no. 9, pp. 4151–4157, 2014.

[4] R. Fiorenza, S. Scirè, and A. M. Venezia, "Carbon supported bimetallic Ru-Co catalysts for H2production through $_{\text{NaBH4and}}$ NH3BH3hydrolysis," *International Journal of Energy Research*, vol. 42, no. 3, pp. 1183–1195, 2018.

[5] M. V. Lototskyy, V. A. Yartys, B. G. Pollet, and R. C. Bowman Jr., "Metal hydride hydrogen compressors: a review," *International Journal of Hydrogen Energy*, vol. 39, no. 11, pp. 5818–5851, 2014.

[6] B. Chettri, P. K. Patra, N. N. Hieu, and D. P. Rai, "Hexagonal boron nitride (h-BN) nanosheet as a potential hydrogen adsorption material: a density functional theory (DFT) study," *Surfaces and Interfaces*, vol. 24, article 101043, 2021.

[7] N. Kostoglou, C. Koczwara, C. Prehal et al., "Nanoporous activated carbon cloth as a versatile material for hydrogen adsorption, selective gas separation and electrochemical energy storage," *Nano Energy*, vol. 40, pp. 49–64, 2017.

[8] Q. L. Zhu and Q. Xu, "Liquid organic and inorganic chemical hydrides for high-capacity hydrogen storage," *Energy & Environmental Science*, vol. 8, no. 2, pp. 478–512, 2015.

[9] Y. Y. Jiang, H. B. Dai, Y. J. Zhong, D. M. Chen, and P. Wang, "Complete and rapid conversion of hydrazine monohydrate to hydrogen over supported Ni–Pt nanoparticles on mesoporous ceria for chemical hydrogen storage," *Chem*, vol. 21, no. 43, pp. 15439–15445, 2015.

[10] I. Cabria, A. Lebon, M. B. Torres, L. J. Gallego, and A. Vega, "Hydrogen storage capacity of Li-decorated borophene and pristine graphene slit pores: a combined ab initio and quantum-thermodynamic study," *Applied Surface Science*, vol. 562, article 150019, 2021.

[11] S. Akbayrak, G. Çakmak, T. Öztürk, and S. Özkar, "Rhodium(0), ruthenium(0) and palladium(0) nanoparticles supported on carbon- coated iron: magnetically isolable and reusable catalysts for hydrolytic dehydrogenation of ammonia borane," *International Journal of Hydrogen Energy*, vol. 46, no. 25, pp. 13548–13560, 2021.

[12] U. B. Demirci, "Mechanistic insights into the thermal decomposition of ammonia borane, a material studied for chemical hydrogen storage," *Inorganic Chemistry Frontiers*, vol. 8, no. 7, pp. 1900–1930, 2021.

[13] Y. Peng, Y. He, Y. Wang, Y. Long, and G. Fan, "Sustainable one-pot construction of oxygen-rich nitrogen-doped carbon nanosheets stabilized ultrafine Rh nanoparticles for efficient ammonia borane hydrolysis," *Journal of Colloid and Interface Science*, vol. 594, pp. 131–140, 2021.

[14] M. Rakap, "Hydrogen generation from hydrolysis of ammonia borane in the presence of highly efficient poly(*N* -vinyl-2-pyrrolidone)-protected platinum-ruthenium nanoparticles," *Applied Catalysis A: General*, vol. 478, pp. 15–20, 2014.

[15] B. Zhao, K. Feng, Y. Wang et al., "PtxNi10−xO nanoparticles supported on N-doped graphene oxide with a synergetic effect for highly efficient hydrolysis of ammonia borane," *Catalysis Science & Technology*, vol. 7, no. 21, pp. 5135–5142, 2017.

[16] F. Y. Zhong, Q. Wang, C. L. Xu et al., "Catalytically active rhodium nanoparticles stabilized by nitrogen doped carbon for the hydrolysis of ammonia borane," *International Journal of Hydrogen Energy*, vol. 43, no. 49, pp. 22273–22280, 2018.

[17] P. P. Zhao, N. Cao, W. Luo, and G. Z. Cheng, "Nanoscale MIL-101 supported RhNi nanoparticles: an efficient catalyst for hydrogen generation from hydrous hydrazine," *Journal of Materials Chemistry A*, vol. 3, no. 23, pp. 12468–12475, 2015.

[18] C. L. Yang, Y. N. Men, Y. Z. Xu, L. J. Liang, P. Cai, and W. Luo, "In situ synthesis of NiCoP nanoparticles supported on reduced graphene oxide for the catalytic hydrolysis of ammonia borane," *ChemPlusChem*, vol. 84, no. 4, pp. 382–386, 2019.

[19] L. Yang, N. Cao, C. Du et al., "Graphene supported cobalt(0) nanoparticles for hydrolysis of ammonia borane," *Materials Letters*, vol. 115, pp. 113–116, 2014.

[20] S. R. Xu, H. T. Zhao, T. S. Li et al., "Iron-based phosphides as electrocatalysts for the hydrogen evolution reaction: recent advances and future prospects," *Journal of Materials Chemistry A*, vol. 8, no. 38, pp. 19729–19745, 2020.

[21] E. J. Popczun, J. R. McKone, C. G. Read et al., "Nanostructured nickel phosphide as an electrocatalyst for the hydrogen evolution reaction," *Journal of the American Chemical Society*, vol. 135, no. 25, pp. 9267–9270, 2013.

[22] M. T. Zhang, S. Q. Ci, H. Li, P. W. Cai, H. M. Xu, and Z. H. Wen, "Highly defective porous CoP nanowire as electrocatalyst for full water splitting," *International Journal of Hydrogen Energy*, vol. 42, no. 49, pp. 29080–29090, 2017.

[23] H. J. Yan, C. G. Tian, L. Wang et al., "Phosphorus-modified tungsten nitride/reduced graphene oxide as a high- performance, non-noble-metal electrocatalyst for the hydrogen evolution reaction," *Angewandte Chemie, International Edition*, vol. 54, no. 21, pp. 6325–6329, 2015.

[24] Y. M. Shi and B. Zhang, "Recent advances in transition metal phosphide nanomaterials: synthesis and applications in hydrogen evolution reaction," *Chemical Society Reviews*, vol. 45, no. 6, pp. 1529–1541, 2016.

[25] X. Q. Du, C. L. Yang, X. Zeng et al., "Amorphous NiP supported on rGO for superior hydrogen generation from hydrolysis of ammonia borane," *International Journal of Hydrogen Energy*, vol. 42, no. 20, pp. 14181–14187, 2017.

[26] C. Y. Peng, L. Kang, S. Cao, Y. Chen, Z. S. Lin, and W. F. Fu, "Nanostructured Ni2P as a robust catalyst for the hydrolytic dehydrogenation of ammonia–borane," *Angewandte Chemie, International Edition*, vol. 54, no. 52, pp. 15725–15729, 2015.

[27] N. I. Kovtyukhova, P. J. Ollivier, B. R. Martin et al., "Layer-by-layer assembly of ultrathin composite films from micron-sized graphite oxide sheets and polycations," *Chemistry of Materials*, vol. 11, no. 3, pp. 771–778, 1999.

[28] S. William, J. R. Hummers, and R. E. Offeman, "Preparation of graphitic oxide," *Journal of the American Chemical Society*, vol. 80, no. 6, pp. 1339–1339, 1958.

[29] Z. X. Yang, F. Y. Cheng, Z. L. Tao, J. Liang, and J. Chen, "Decreasing the thermal dehydrogenation temperature of methylamine borane (MeAB) by mixing with poly(methyl acrylate) (PMA)," *International Journal of Hydrogen Energy*, vol. 37, no. 9, pp. 7638–7644, 2012.

[30] H. L. Jiang, T. Akita, and Q. Xu, "A one-pot protocol for synthesis of non-noble metal-based core–shell nanoparticles under ambient conditions: toward highly active and cost-effective catalysts for hydrolytic dehydrogenation of NH_3BH_3," *Chemical Communications*, vol. 47, no. 39, pp. 10999–11001, 2011.

[31] H. L. Wang, J. T. Robinson, X. L. Li, and H. J. Dai, "Solvothermal reduction of chemically exfoliated graphene sheets," *Journal of the American Chemical Society*, vol. 131, no. 29, pp. 9910-9911, 2009.

[32] S. K. Kim, T. J. Kim, T. Y. Kim et al., "Tetraglyme-mediated synthesis of Pd nanoparticles for dehydrogenation of ammonia borane," *Chemical Communications*, vol. 48, no. 14, pp. 2021–2023, 2012.

[33] H. L. Wang, L. F. Cui, Y. Yang et al., "Mn_3O_4–graphene hybrid as a high-capacity anode material for lithium ion batteries," *Journal of the American Chemical Society*, vol. 132, no. 40, pp. 13978–13980, 2010.

[34] Y. W. Yang, Z. H. Lu, Y. Hu et al., "Facile in situ synthesis of copper nanoparticles supported on reduced graphene oxide for hydrolytic dehydrogenation of ammonia borane," *RSC Advances*, vol. 4, no. 27, pp. 13749–13752, 2014.

[35] P. X. Xi, F. J. Chen, G. Q. Xie et al., "Surfactant free RGO/Pd nanocomposites as highly active heterogeneous catalysts for the hydrolytic dehydrogenation of ammonia borane for chemical hydrogen storage," *Nanoscale*, vol. 4, no. 18, pp. 5597–5601, 2012.

[36] C. Tang, R. Zhang, W. B. Lu et al., "Energy-saving electrolytic hydrogen generation: Ni2P nanoarray as a high- performance non-noble-metal electrocatalyst," *Angewandte Chemie, International Edition*, vol. 56, no. 3, pp. 842–846, 2017.

[37] Z. Q. Wang, Y. L. Chen, Y. T. He, W. D. Jiang, Y. Long, and G. Y. Fan, "Facile construction of composition-tuned ruthenium-nickel nanoparticles on g-C_3N_4 for enhanced hydrolysis of ammonia borane without base additives," *International Journal of Hydrogen Energy*, vol. 46, no. 21, pp. 11587–11596, 2021.

[38] Y. M. Shi, Y. Xu, S. F. Zhuo, J. F. Zhang, and B. Zhang, "Ni_2P nanosheets/Ni foam composite electrode for long-lived and pH-tolerable electrochemical hydrogen generation," *ACS Applied Materials & Interfaces*, vol. 7, no. 4, pp. 2376–2384, 2015.

[39] L. A. Stern, L. G. Feng, F. Song, and X. L. Hu, "Ni_2P as a Janus catalyst for water splitting: the oxygen evolution activity of Ni_2P nanoparticles," *Energy & Environmental Science*, vol. 8, no. 8, pp. 2347–2351, 2015.

[40] M. X. Duan, Q. Y. Cheng, M. M. Wang, and Y. J. Wang, "In situ hydrodeoxygenation of vanillin over Ni–Co–P/HAP with formic acid as a hydrogen source," *RSC Advances*, vol. 11, no. 18, pp. 10996–11003, 2021.

[41] W. Li, X. F. Gao, X. G. Wang et al., "From water reduction to oxidation: Janus Co-Ni-P nanowires as high-efficiency and ultrastable electrocatalysts for over 3000 h water splitting," *Journal of Power Sources*, vol. 330, pp. 156–166, 2016.

[42] Z. H. Pu, Q. Liu, C. Tang, A. M. Asiri, and X. Sun, "Ni_2P nanoparticle films supported on a Ti plate as an efficient hydrogen evolution cathode," *Nanoscale*, vol. 6, no. 19, pp. 11031–11034, 2014.

[43] L. Cui, Y. H. Xu, L. Niu, W. R. Yang, and J. Q. Liu, "Monolithically integrated CoP nanowire array: an on/off switch for effective on-demand hydrogen generation via hydrolysis of $NaBH_4$ and NH_3BH_3," *Nano Research*, vol. 10, no. 2, pp. 595–604, 2017.

[44] X. N. Chen, X. H. Wang, and D. Fang, "A review on C1s XPS-spectra for some kinds of carbon materials," *Fullerence, Nanotubes, and Carbon Nanostructures*, vol. 28, no. 12, pp. 1048–1058, 2020.

[45] S. Akbayrak, M. Kaya, M. Volkan, and S. Özkar, "Palladium(0) nanoparticles supported on silica-coated cobalt ferrite: a highly active, magnetically isolable and reusable catalyst for hydrolytic dehydrogenation of ammonia borane," *Applied Catalysis. B, Environmental*, vol. 147, pp. 387–393, 2014.

[46] G. Z. Chen, S. Desinan, R. Rosei, F. Rosei, and D. Ma, "Synthesis of Ni–Ru alloy nanoparticles and their high catalytic activity in dehydrogenation of ammonia borane," *Chemistry - A European Journal*, vol. 18, no. 25, pp. 7925–7930, 2012.

[47] Q. T. Wang, Z. Zhang, J. Liu, R. C. Liu, and T. Liu, "Bimetallic non-noble CoNi nanoparticles monodispersed on multiwall carbon nanotubes: highly efficient hydrolysis of ammonia borane," *Materials Chemistry and Physics*, vol. 204, pp. 58–61, 2018.

[48] B. Qu, Y. Tao, L. Yang, and Y. Liu, "One-pot co-reduction synthesis of orange-like Pd@Co@P nanoparticles supported on rGO for catalytic hydrolysis of ammonia borane," *International Journal of Hydrogen Energy*, vol. 46, no. 61, pp. 31324–31333, 2021.

[49] H. Çelik Kazici, F. Yildiz, M. S. İzgi, B. Ulaş, and H. Kivrak, "Novel activated carbon supported trimetallic PdCoAg nanoparticles as efficient catalysts for the hydrolytic dehydrogenation of ammonia borane," *International Journal of Hydrogen Energy*, vol. 44, no. 21, pp. 10561–10572, 2019.

[50] J. Manna, S. Akbayrak, and S. Özkar, "Nickel(0) nanoparticles supported on bare or coated cobalt ferrite as highly active, magnetically isolable and reusable catalyst for hydrolytic dehydrogenation of ammonia borane," *Journal of Colloid and Interface Science*, vol. 508, pp. 359–368, 2017.

[51] J. Wang, Y. L. Qin, X. Liu, and X. B. Zhang, "In situ synthesis of magnetically recyclable graphene-supported Pd@Co core–shell nanoparticles as efficient catalysts for hydrolytic dehydrogenation of ammonia borane," *Journal of Materials Chemistry A*, vol. 22, no. 25, p. 12468, 2012.

[52] N. S. Çiftci and Ö. Metin, "Monodisperse nickel-palladium alloy nanoparticles supported on reduced graphene oxide as highly efficient catalysts for the hydrolytic dehydrogenation of ammonia borane," *International Journal of Hydrogen Energy*, vol. 39, no. 33, pp. 18863–18870, 2014.

[53] N. Wang, Q. M. Sun, R. S. Bai, X. Li, G. Q. Guo, and J. H. Yu, "In situ confinement of ultrasmall Pd clusters within nanosized silicalite-1 zeolite for highly efficient catalysis of hydrogen generation," *Journal of the American Chemical Society*, vol. 138, no. 24, pp. 7484–7487, 2016.

[54] O. Ozay, E. Inger, N. Aktas, and N. Sahiner, "Hydrogen production from ammonia borane via hydrogel template synthesized Cu, Ni, Co composites," *International Journal of Hydrogen Energy*, vol. 36, no. 14, pp. 8209–8216, 2011.

[55] W. W. Zhan, Q. L. Zhu, and Q. Xu, "Dehydrogenation of ammonia borane by metal nanoparticle catalysts," *ACS Catalysis*, vol. 6, no. 10, pp. 6892–6905, 2016.

[56] Y. T. Wang, G. Q. Shen, Y. X. Zhang, L. Pan, X. W. Zhang, and J.-J. Zou, "Visible-light-induced unbalanced charge on NiCoP/TiO_2 sensitized system for rapid H_2 generation from hydrolysis of ammonia borane," *Applied Catalysis B: Environmental*, vol. 260, article 118183, 2020.